Formation of Self-Organized Mn$_3$O$_4$ Nanoinclusions in LaMnO$_3$ Films

Alberto Pomar[1]*, Zorica Konstantinović[2], Núria Bagués[1,3], Jaume Roqueta[3], Laura López-Mir[1], Lluis Balcells[1], Carlos Frontera[1], Narcis Mestres[1], Araceli Gutiérrez-Llorente[4], Maja Šćepanović[2], Nenad Lazarević[2], Zoran V. Popović[2], Felip Sandiumenge[1], Benjamín Martínez[1] and José Santiso[3]

[1] Instituto de Ciencia de Materiales de Barcelona-Consejo Superior de Investigaciones Científicas, Bellaterra, Spain, [2] Center for Solid State Physics and New Materials, Institute of Physics Belgrade, University of Belgrade, Belgrade, Serbia, [3] Catalan Institute of Nanoscience and Nanotechnology, Consejo Superior de Investigaciones Científicas and The Barcelona Institute of Science and Technology, Bellaterra, Spain, [4] ESCET, Universidad Rey Juan Carlos, Madrid, Spain

We present a single-step route to generate ordered nanocomposite thin films of secondary phase inclusions (Mn$_3$O$_4$) in a pristine perovskite matrix (LaMnO$_3$) by taking advantage of the complex phase diagram of manganese oxides. We observed that in samples grown under vacuum growth conditions from a single LaMnO$_3$ stoichiometric target by Pulsed Laser Deposition, the most favorable mechanism to accommodate Mn^{2+} cations is the spontaneous segregation of self-assembled wedge-like Mn$_3$O$_4$ ferrimagnetic inclusions inside a LaMnO$_3$ matrix that still preserves its orthorhombic structure and its antiferromagnetic bulk-like behavior. A detailed analysis on the formation of the self-assembled nanocomposite films evidences that Mn$_3$O$_4$ inclusions exhibit an epitaxial relationship with the surrounding matrix that it may be explained in terms of a distorted cubic spinel with slight (∼9°) c-axis tilting. Furthermore, a Ruddlesden-Popper La$_2$MnO$_4$ phase, helping to the stoichiometry balance, has been identified close to the interface with the substrate. We show that ferrimagnetic Mn$_3$O$_4$ columns influence the magnetic and transport properties of the nanocomposite by increasing its coercive field and by creating local areas with enhanced conductivity in the vicinity of the inclusions.

Keywords: self-organization, nanocomposite, LaMnO$_3$, oxide thin films, strain effects

INTRODUCTION

The large choice in chemical elements in either A- and B-site of the perovskite structure allows tailoring many parameters including lattice constants, electronic band structures, magnetic interactions, and more. In particular, manganese based oxides display a huge range of properties from total spin polarization and colossal magnetoresistance to multiferroicity, with potential use from active electrodes in electronic devices to sensors and magnetic memories. Furthermore, nanostructured thin films widen their application range as their final functional properties are determined by the very active role of interfaces and surfaces which may be efficiently modified by strain relaxation mechanisms [1–4]. Specially in the case of undoped LaMnO$_3$ (LMO), the appearance of ferromagnetism in heterostructures of LaMnO$_3$/SrTiO$_3$ [5] and LaMnO$_3$/SrMnO$_3$ [6], or the observation of exchange bias in LaMnO$_3$/LaNiO$_3$ superlattices [7] evidence the importance of interfacial phenomena. In addition to standard heterointerfaces in layered structures, new strategies have been developed to increase the surface to volume ratio and to enhance interfacial effects. In this sense, vertically heteroepitaxial nanocomposites (VHN) provide

a vertical contact area between two immiscible compounds much larger than substrate to films. Additionally, lateral strain may be tuned to large film thicknesses [8].

Spontaneous organization of vertical heteroepitaxial nanocomposite thin films has enabled the discovery of new physical phenomena at the nanoscale and their possible use in magnetoelectric devices. For instance, large adjustable low-field magnetoresistance is observed in vertically aligned La$_{0.7}$Ca$_{0.3}$MnO$_3$ [9] or La$_{0.7}$Sr$_{0.3}$MnO$_3$ (LSMO) based nanocomposites [10, 11]. A good example of this is the system LSMO:Mn$_3$O$_4$ that has been often proposed as potential nanocomposite due to the chemical compatibility of Mn$_3$O$_4$ with the whole manganite perovskite family [12]. Indeed, if the composition ratio [La+Sr]/[Mn] < 1, a spinodal decomposition mechanism in chemical solution deposited films may lead to the spontaneous formation of LSMO:Mn$_3$O$_4$ VHNs [13]. The so-generated vertical lattice strain is found to be related to the different domain and grain boundary structures and directly impact their ferromagnetic properties [11]. In the particular case of the parent compound, i.e., undoped LaMnO$_3$, manganese segregation is expected to occur when La deficiency leads to a non-stoichiometric ratio of La/Mn < 0.9 [14]. There, the appearance of randomly distributed segregates of manganese oxides such as Mn$_3$O$_4$ or MnO has been reported in bulk samples [15, 16] and thin films [17]. It is important, from a fundamental point of view, to understand the formation of manganese oxide segregates, as it is a characteristic secondary phase in several REMnO$_3$ (RE = Rare Earth) thin films and heterostructures, thus modifying their structural quality and functional properties [18–20]. Furthermore, manganese oxides are extremely attractive for potential applications due to their electrochemical, optical, or catalytic properties [21–24]. In spite of their abundance in nature reproducible properties of manganese oxides require the fabrication of uniform structures and a large effort is devoted to produce MnO$_x$ nanostructures (for recent Reviews see, for example, [23, 24] and references therein). In the present study, we report on the spontaneous formation of regular vertically aligned nanocolumns composed of manganese oxide embedded in antiferromagnetic LaMnO$_3$ matrix grown by pulsed laser deposition (PLD) on (001)-oriented single crystal perovskite substrates of LaAlO$_3$ (LAO) and SrTiO$_3$ (STO). The formation mechanisms of the manganese oxide secondary phase and their influence on functional properties of manganite thin films are discussed in detail.

MATERIALS AND METHODS

LaMnO$_3$ and Mn$_3$O$_4$

The primary phase i.e., the matrix in the studied films is LaMnO$_3$ (LMO) which in its stoichiometric bulk state is an antiferromagnetic insulator with T$_N$ ~140 K [25, 26]. The crystal structure of the bulk LMO is described by an orthorhombic Pbnm space group with cell parameters a = 5.533 Å, b = 5.727 Å, and c = 7.668 Å at room temperature [26]. Achieving the right LaMnO$_3$ stoichiometry in thin films leading to an antiferromagnetic (AF) ground state remains challenging regardless of the growth technique and it requires a fine control

of growth conditions [27]. In particular, AF behavior is only obtained in films prepared at low oxygen pressures while the right stoichiometry is maintained. In fact, deviations from [La]/[Mn] = 1 stoichiometry in LMO thin films may easily change Mn oxidation state leading to ferromagnetic behavior [28, 29]. The secondary phase in films is the manganese oxide MnO$_x$ which could present mixed Mn oxidation states (Mn^{2+}, Mn^{3+}, or even Mn^{4+}). In general, manganese may easily alter its valence forming different oxide stoichiometries in response to the environmental conditions. Under thermodynamic equilibrium, bulk oxide stoichiometries are directly determined by oxygen partial pressure and temperature. In the vacuum conditions used in the present work either MnO, Mn$_3$O$_4$, or Mn$_2$O$_3$ may be formed depending on the residual oxygen partial pressure in the chamber [17]. At the growth temperature of 850°C, Mn^{2+}O should be thermodynamically favored if P(O$_2$) < 2 × 10^{-4} mTorr while Mn$_2^{3+}$O$_3$ is only expected for oxygen pressures close to atmospheric conditions (α-Mn$_2$O$_3$ being the usual polymorph phase while γ-Mn$_2$O$_3$ has been observed in nanometric form [30]). At intermediate pressures, the mixed valence manganese oxide Mn$_3$O$_4$ (or Mn^{2+}Mn$_2^{3+}$O$_4$ in spinel notation) is expected to be the dominant phase [31]. The different oxides are quite difficult to distinguish and share several characteristic features. Manganese oxides as Mn$_3$O$_4$, or γ-Mn$_2$O$_3$ are ferrimagnetic with transition temperature, T$_c$, around 40 K while MnO and α-Mn$_2$O$_3$ exhibit antiferromagnetic ordering below 118 and 80 K, respectively [30, 32, 33]. Regarding their crystal structure, MnO is a cubic rocksalt with a = 4.45 Å [34], α-Mn$_2$O$_3$ is cubic bixbyite (a = 9.42 Å) while Mn$_3$O$_4$ and γ-Mn$_2$O$_3$ exhibit spinel-like structures. Mn$_3$O$_4$ is hausmannite mineral with distorted spinel structure with manganese ions placed on two non-equivalent tetrahedral (Mn^{2+}) and octahedral (Mn^{3+}) sites. The structure is well described by tetragonal I4$_1$/amd space group with cell parameters of a = 5.76 Å and c = 9.47 Å [35, 36]. A very similar spinel structure is reported for γ-Mn$_2$O$_3$ with a = 5.79 Å and c = 9.40 Å [30]. As each of these oxides have cubic or tetragonal symmetry they can epitaxially grow on cubic perovskite substrates under suitable conditions. Furthermore, biaxial strain (either compressive or tensile) may modify not only their equilibrium phase diagram but it also may lead to the appearance of other crystal structures as, for example, the high pressure Mn$_3$O$_4$ cubic phase [37–39]. This epitaxial stabilization reported on MgO substrates was not observed for Mn$_3$O$_4$ films grown on STO or LAO due to the large compressive mismatch of (a$_{Mn3O4}$/$\sqrt{2}$-a$_{STO}$)/a$_{STO}$ = −4% and (a$_{Mn3O4}$/$\sqrt{2}$-a$_{LAO}$)/a$_{LAO}$ = −7% [40]. However, in VHNs where lateral strain imposed by the surrounding oxide matrix may add a supplementary gain to the free energy balance, the formation of Mn$_3$O$_4$ cubic phase has been recently reported [13, 41].

Experimental Methods

Thin films of LaMnO$_3$ with self-assembled manganese oxide nanocolumns have been prepared from stoichiometric LaMnO$_3$ ceramic targets by PLD with a KrF excimer laser. A spontaneous assembly of manganese oxide nanocolumns has been observed at 850°C under vacuum conditions (background pressure of <5 × 10^{-4} mTorr). The laser fluency was kept below <1 J/cm^2

with 10 Hz pulse repetition rate. The films were grown on top of SrTiO$_3$ (100) and LaAlO$_3$ (100) substrates and their thickness are kept between 30 and 100 nm as determined by X-ray reflectometry.

The structural characterization was carried out by X-ray diffraction using a four-angle diffractometer with a Cu-K$_\alpha$ radiation source (X'Pert Pro MRD-Panalytical). All the structural drawings and schemes were produced by using VESTA program [42].

The detailed microstructure and the chemical composition was investigated by Transmission Electron Microscopy (TEM) observations of cross section specimens of LMO/STO on a FEI Tecnai G^2 F20 S-TWIN HR(S)TEM operated at 200 kV. Cross section specimens were prepared by conventional cutting, gluing and grinding procedures followed by an Ar-ion milling step down to electron transparency by Precision Ion Polishing System (PIPS^{TM})—Gatan. High annular dark field (HAADF) images, energy dispersive X-ray spectroscopy (EDS) profiles and electron energy loss spectroscopy (EELS) spectrum—images (SI) were obtained to identify the composition of the nanopillars. EELS-SI of cross-section samples was also carried out in DualEELS mode with a Titan3^{TM} G2 60-300 operating at 300 kV, equipped with a Dual-EELS spectrometer. The principal components analysis (PCA) provided by Lucas et al. [43] for Digital Micrograph was used to remove the random noise. The power law was used before energy peak to remove the background and then data was deconvolved using the Fourier Log method. The La/Mn ratio was obtained from EDS of areas in the matrix tilting the sample out-of-zone axis in order to minimize the electron channeling. High resolution TEM images obtained from selected regions in the micrograph (the matrix, the nanopillar, and the interface between them) were used to identify the matrix orientation and the manganese oxide phase of the inclusions using the Eje-Z software [44].

The surface morphology was studied by Scanning Electron Microscopy (SEM) using a QUANTA FEI 200 FEG-ESEM microscope. Measurements of the local electrical conductivity were performed by Conducting-Atomic Force Microscopy (c-AFM) using a MFP-3D Asylum and ORCA module. A conductive tip with PtIr coating was used as a top electrode and the voltage was applied directly to the sample. A constant nominal force of 3 N/m was used in tapping mode. The topography and current maps were acquired simultaneously.

The magnetic properties were measured in a commercial SQUID magnetometer (Quantum Design). The magnetic field was applied parallel to the substrate in all measurements. The substrate diamagnetic contribution is evaluated from the field dependence of the magnetization at room temperature and systematically subtracted from the measurements.

Raman scattering measurements were performed using a TriVista 557 Raman system equipped with a nitrogen-cooled CCD detector, in backscattering micro-Raman configuration. The 532 nm line of the Verdi G laser was used as an excitation source. A microscope objective with 100 magnification was used for focusing the laser beam. All measurements were carried out at low laser power, in order to minimize local heating of the sample. Raman scattering measurements at temperatures lower
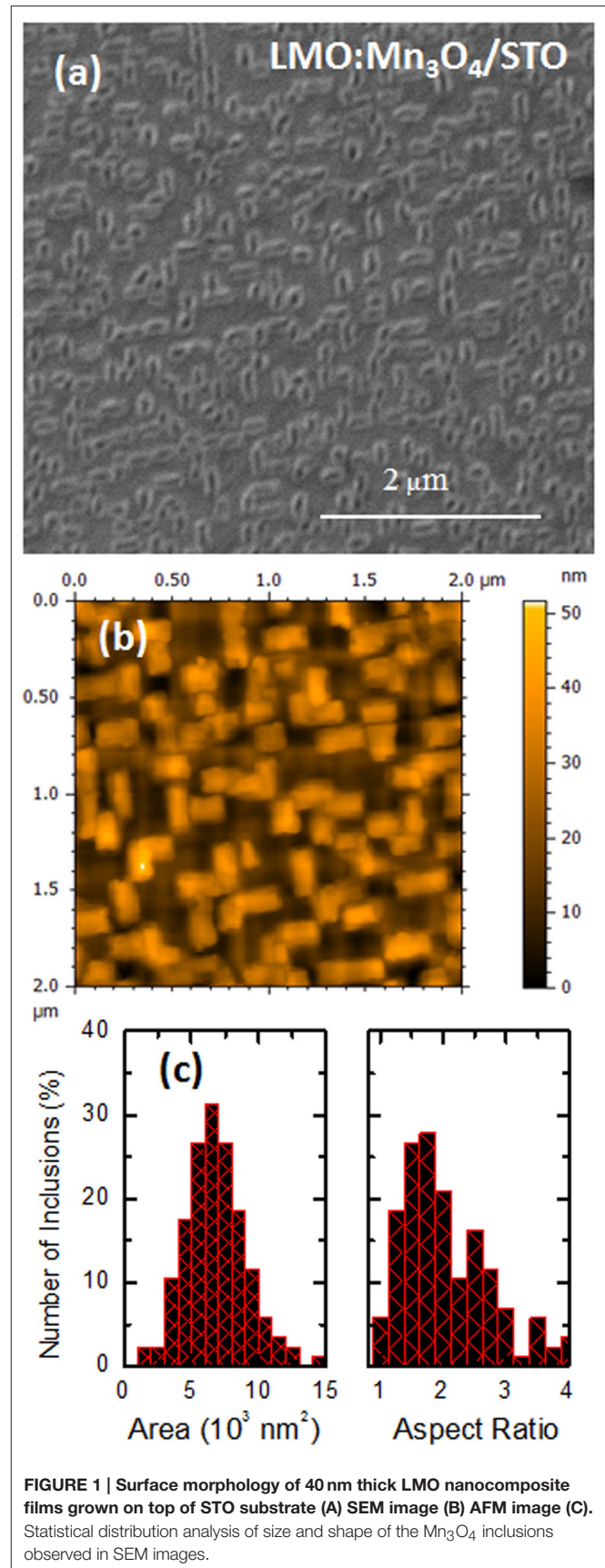
FIGURE 1 | Surface morphology of 40 nm thick LMO nanocomposite films grown on top of STO substrate (A) SEM image (B) AFM image (C). Statistical distribution analysis of size and shape of the Mn$_3$O$_4$ inclusions observed in SEM images.

than room temperature were performed in the back-scattering geometry in a cryostat system using 488-nm line of an Ar$^+$ laser, Jobin–Yvon U1000 double monochromator, and photomultiplier as detector.

The experimental results presented in this work were obtained on the exact same samples, either on LAO or STO substrates with the only exception of temperature dependent Raman measurements where, to enhance signal to background ratio, a thicker sample grown on LAO (∼100 nm) was used.
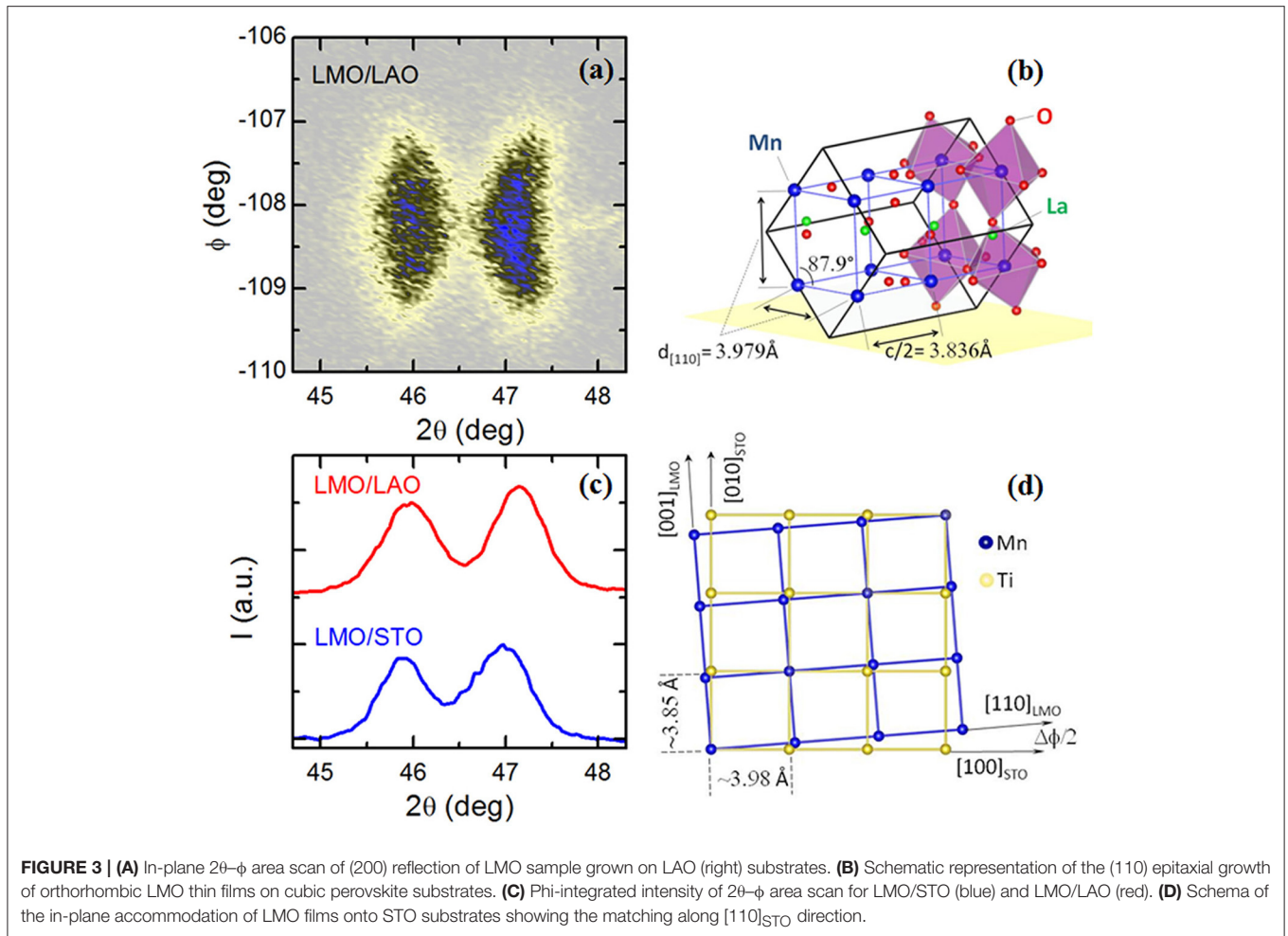
RESULTS AND DISCUSSION

Films grown in vacuum conditions exhibit a clear ordered nanocomposite surface, as evidenced by SEM images either on STO or LAO substrates (see **Figures 1A**, **2A**, respectively). It is observed that the inclusions of the secondary phase (manganese oxide) are uniformly distributed in the LMO matrix (primary phase) with typical rectangular-based dimensions of 40 × 150 nm (on STO substrate) and 40 × 90 nm (on LAO substrate). It is worth reminding here that this spontaneous regular formation of manganese oxide in LMO thin films has been obtained by laser ablation of single target and it is linked to the low oxidation conditions during the PLD process. Films grown at higher oxygen pressures exhibit flat surfaces with no sign of phase segregation [27]. More information about the arrangement of the secondary phase may be obtained from atomic force microscopy images as the shown in **Figure 1B** (on STO) and **Figure 2B** (on LAO). While the manganite LMO phase appears to be very flat with low roughness (rms < 0.5 nm), MnO$_x$ nanopillars appear as large inclusions exceeding the surface of the matrix by several nm. From this preliminary characterization we may estimate that secondary phase occupies around 10–15% of the total surface, as determined by quantifying black areas (different chemical composition) in the SEM images. An interesting observation is that MnO$_x$ inclusions are mainly oriented with their rectangular sides aligned with the main axes of the substrates. Statistical analysis of the inclusions is presented in the histograms of **Figures 1C** and **2C**. We may see that size and aspect ratio is enhanced in the case of films grown on STO substrates. This suggests that the different mismatch with substrate plays a role in the statistical size distribution of the segregates.

As mentioned above, epitaxial growth of orthorhombic stoichiometric LMO films has been studied by several groups in the past to elucidate the controversial appearance of ferromagnetic behavior. Either strain or oxygen content has been claimed to be at the origin of this anomalous magnetic behavior [28, 29, 45–49]. In LMO bulk state, oxygen off-stoichiometry (in fact, cation vacancy) is accommodated by modifying the Mn-O octahedral environment mainly resulting in a strong change in the orthorhombic lattice parameters that also influences the cooperative Jahn-Teller effect and, as a result, the magnetic ordering. Quite recently we have shown that a careful epitaxial analysis is required to fully understand the growth of LMO films under different oxygen conditions [27]. For this reason, we have performed reciprocal 2θ–φ area scans at grazing incidence around 220 and 004 orthorhombic in-plane reflections (corresponding to 200 reflections in
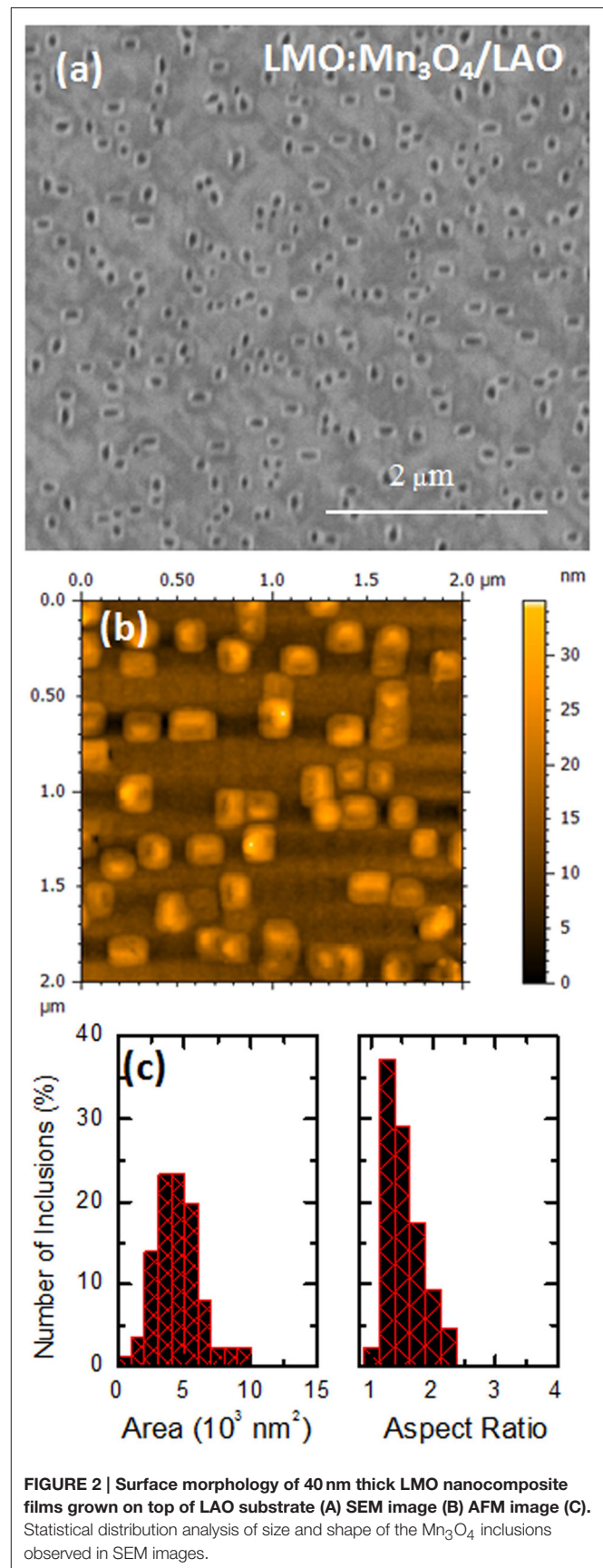
FIGURE 2 | Surface morphology of 40 nm thick LMO nanocomposite films grown on top of LAO substrate (A) SEM image **(B)** AFM image **(C).** Statistical distribution analysis of size and shape of the Mn$_3$O$_4$ inclusions observed in SEM images.

FIGURE 3 | (A) In-plane 2θ–φ area scan of (200) reflection of LMO sample grown on LAO (right) substrates. **(B)** Schematic representation of the (110) epitaxial growth of orthorhombic LMO thin films on cubic perovskite substrates. **(C)** Phi-integrated intensity of 2θ–φ area scan for LMO/STO (blue) and LMO/LAO (red). **(D)** Schema of the in-plane accommodation of LMO films onto STO substrates showing the matching along [110]$_{STO}$ direction.
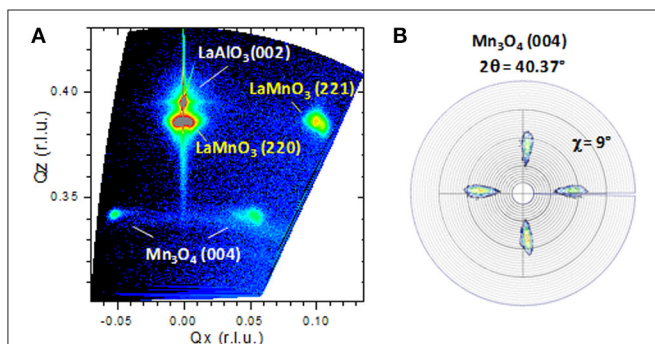
pseudocubic notation). **Figure 3A** shows a typical area scan for LMO sample grown on LAO. Similar results were obtained previously for films grown on STO [27]. We observe the presence of two peaks occurring at different 2θ angles that are the clear signature of twinned domains with two in-plane lattice parameters. To understand this result, we need to consider that growth temperature (T$_g$ = 1123 K) is well above Jahn-Teller transition of LMO (T$_{JT}$ = 750 K) and, although still exhibiting Pbnm crystallographic structure, all orthorhombic LMO matching distances are nearly equal (a$_{LMO798K}$/$\sqrt{2}$ = 3.9468 Å, b$_{LMO798K}$/$\sqrt{2}$ = 3.9478 Å, c$_{LMO798K}$ = 3.9448 Å) [50]. Thus, LMO structure is metrically cubic and a cube-on-cube epitaxial relationship with substrate is expected. During cooling, cooperative Jahn-Teller transition takes place in LMO and its MnO$_6$ octahedral framework is extremely distorted (Mn-O bond distances being 1.903, 1.957, and 2.184 Å). To accommodate this structural distortion to the underlying substrate lattice, film may adopt either (110) or (001) orientation. In such situation, it is useful to consider the area mismatch in the basal plane, i.e., $\varepsilon_{area}(110) = \left(d^2_{[110]f} - a^2_s\right)/a^2_s$ for (110)-orientation and $\varepsilon_{area}(001) = \left(d_{[110]f}c_f/2 - a^2_s\right)/a^2_S$ for (001) orientation, where f and s indicate film and substrate, respectively, and d$_{[110]}$ =

(a^2+b^2)$^{1/2}$/2. We may see that $\varepsilon_{area}[110]_{STO}$ = −0.1% and $\varepsilon_{area}[001]_{STO}$ = −3.7% for STO and $\varepsilon_{area}[110]_{LAO}$ = −5.9% and $\varepsilon_{area}[001]_{LAO}$ = −9.3% for LAO. In both cases, (110) orientation shows clearly a better matching which very likely favors this orientation. In this case, when LMO c-axis is contained in the plane of the substrate, we have two different in-plane Mn-Mn matching distances, d$_{[110]LMO}$ = 3.982 Å and d$_{[001]LMO}$ = c$_{LMO}$/2 = 3.834 Å (see schema in **Figure 3B**) leading to twinned domains and the two peaks in **Figure 3A**. A reliable quantitative analysis of the in-plane cell parameters has been performed by integrating the intensity of the respective area scans along the azimuthal angle phi and fitting the corresponding peaks (see **Figure 3C**). We have obtained values of 3.952 and 3.875 Å (on STO) and 3.947 and 3.857 Å (on LAO) for d$_{[110]LMO}$ and d$_{[001]LMO}$, respectively. The resulting effective strains are approximately −1% compressive and 1% tensile for STO and −4 and −2% compressive for LAO substrate. These values of residual strain and in-plane lattice parameters indicate that the LMO thin films grown under vacuum conditions are almost in a relaxed state. In the case of the films grown on STO, such relaxed state may be understood if we calculate the corresponding diagonal basal distances of STO, d$_{[110]STO}$ = 5.523 Å and film, d$_{LMO}$ = 5.534 Å which show a mismatch of 0.3%. This suggests
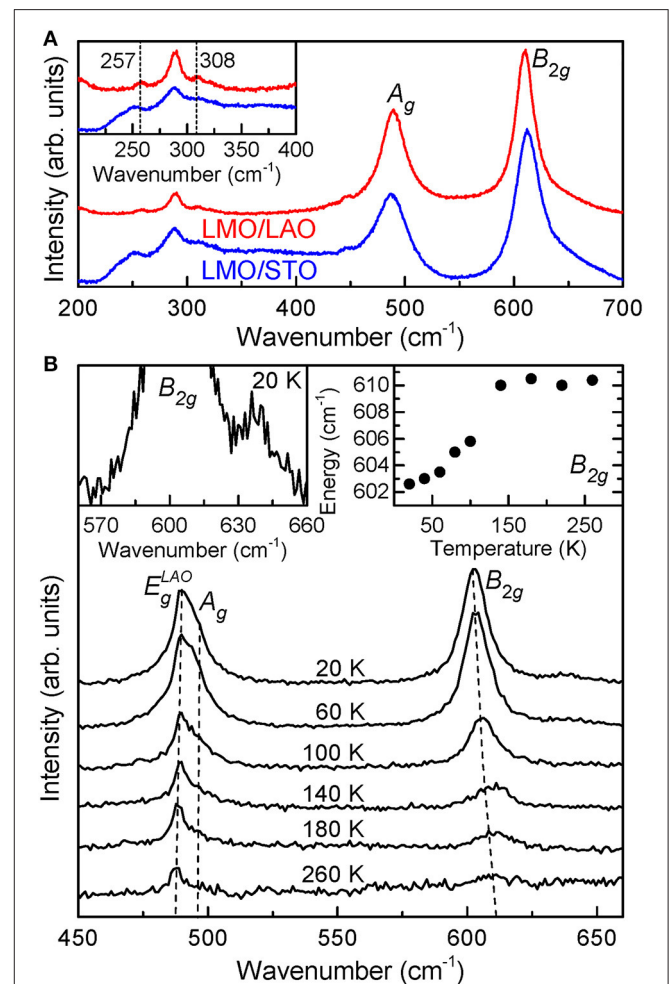
that LMO tends to accommodate to the underlying substrate along STO[110] direction, i.e., in-plane LMO c-axis is slightly rotated with respect to substrate principal axes (see scheme in **Figure 3D**) which is characteristic of the formation of LMO twined domains being the twin boundary plane aligned with the [110]STO direction. The formation of these twin domains takes place during the cooling down process below the Jahn–Teller transition temperature. From standard θ–2θ x-ray diffraction measurements we have also determined the pseudocubic LMO out-of-plane cell parameter, obtaining 3.985 Å for LMO on STO and a larger value of 4.006 Å for LMO on LAO. In both cases, our estimation of pseudocubic unit cell volume leads to ~61 Å^3, close to the expected bulk value for orthorhombic stoichiometric LMO [26]. The relative orientations of film and substrate were also observed by X-ray diffraction reciprocal space maps, as depicted in **Figure 4A**. The map shows the area around the main symmetrical 002 reflection of LaAlO$_3$ substrate. The position of the main film peak close to the substrate peak is compatible with 220 LMO, which corresponds to $c_\parallel$-oriented domains. The observation of 221 LMO reflection indicates the formation of orthorhombic *Pbnm* LMO (which corresponds to half order 2 0 ½ reflection in cubic primitive notation). The fact that half order reflection lies along Q_x direction supports the $c_\parallel$-orientation of the LMO. The two separate reflections at lower Q_z values are consistent with 004 reflections from Mn$_3$O$_4$ spinel with their c-axis tilted 9° at both sides of the vertical direction. The corresponding pole figure of this 004 Mn$_3$O$_4$ reflection is depicted in **Figure 4B** showing the presence of four reflections at χ ~9° separated by φ = 90°. This indicates the textured orientation of Mn$_3$O$_4$ inclusions within the LMO matrix.

Further confirmation that partially relaxed LMO films still preserve orthorhombic symmetry has been obtained by studying the Raman response. **Figure 5A** shows the Raman spectra of LMO nanostructured films at room temperature. In both spectra the same peaks are observed. Those found at frequencies of 257, 244, and 481 cm^{-1} are associated to A_g symmetry whereas those at 308 and 611 cm^{-1} correspond to Raman frequency of B_{2g} symmetry. All of them are fully

compatible with those of orthorhombic LaMnO$_3$ reported for stoichiometric single crystals [51]. Temperature dependence of Raman response for LMO samples grown on LAO substrates is presented in **Figure 5B**. The most pronounced features in the Raman spectra of LMO/LAO sample in the range of 450–660 cm^{-1} correspond to the E_g Raman mode of LAO substrate and to the modes of A_g and B_{2g} symmetry of orthorhombic LMO structure. Note that with lowering of the temperature, B_{2g} Raman mode shows characteristic softening in the antiferromagnetic phase [52], as shown in the right inset of **Figure 5B**. Besides, a low-intensity peak at about 640 cm^{-1}, better discerned in the Raman spectra collected at low temperatures (**Figure 5B**, left inset), can be attributed to the stretching vibration of Mn–O bond in the MnO$_6$ unit of manganese oxide, possibly nanocrystalline Mn$_3$O$_4$. Namely, due to phonon confinement effect, with decreasing mean crystallite size the A_{1g} Raman mode in nanostructured Mn$_3$O$_4$ gradually redshifts compared to its position in bulk

FIGURE 4 | **(A)** X-ray diffraction reciprocal space map around the 220 LaMnO$_3$ and 002 LaAlO$_3$ main reflections showing the presence of 221 half order reflection of $c_\parallel$-LaMnO$_3$, and the presence of 9°-tilted $c_\wedge$ Mn$_3$O$_4$ domains. **(B)** Pole figure of the 004 Mn$_3$O$_4$ reflection showing the four-fold symmetry of the Mn$_3$O$_4$ inclusions.

FIGURE 5 | **(A)** Raman shift at room temperature from corresponding samples of LMO samples grown on STO (blue) and LAO (red) substrates. **(B)** Raman spectra of LMO/LAO sample at low temperatures. Right inset: Temperature dependence of B_{2g} wavenumber. Left inset: Enlarged part of Raman spectrum measured at 20 K.

crystal (~656 cm^{-1}) [53]. In the case of γ-Mn$_2$O$_3$, the main Raman feature is reported to appear at 628 cm^{-1} and, thus, it cannot explain our results of **Figure 5B** [54]. So, the appearance of the Raman mode at ~640 cm^{-1} could be related to the presence of Mn$_3$O$_4$ nanocrystallites with mean size of about 30 nm.

The microstructural analysis on the formation of the MnO$_x$ secondary phase ordered nanostructures, their correlation with substrate/film interface and the relaxation of strain was studied in detail by cross-section TEM (**Figure 6**). The TEM images reveal a wedge-like shape of the nanopillars. Surprisingly, MnO$_x$ columns do not reach the interface with the substrate. However, there
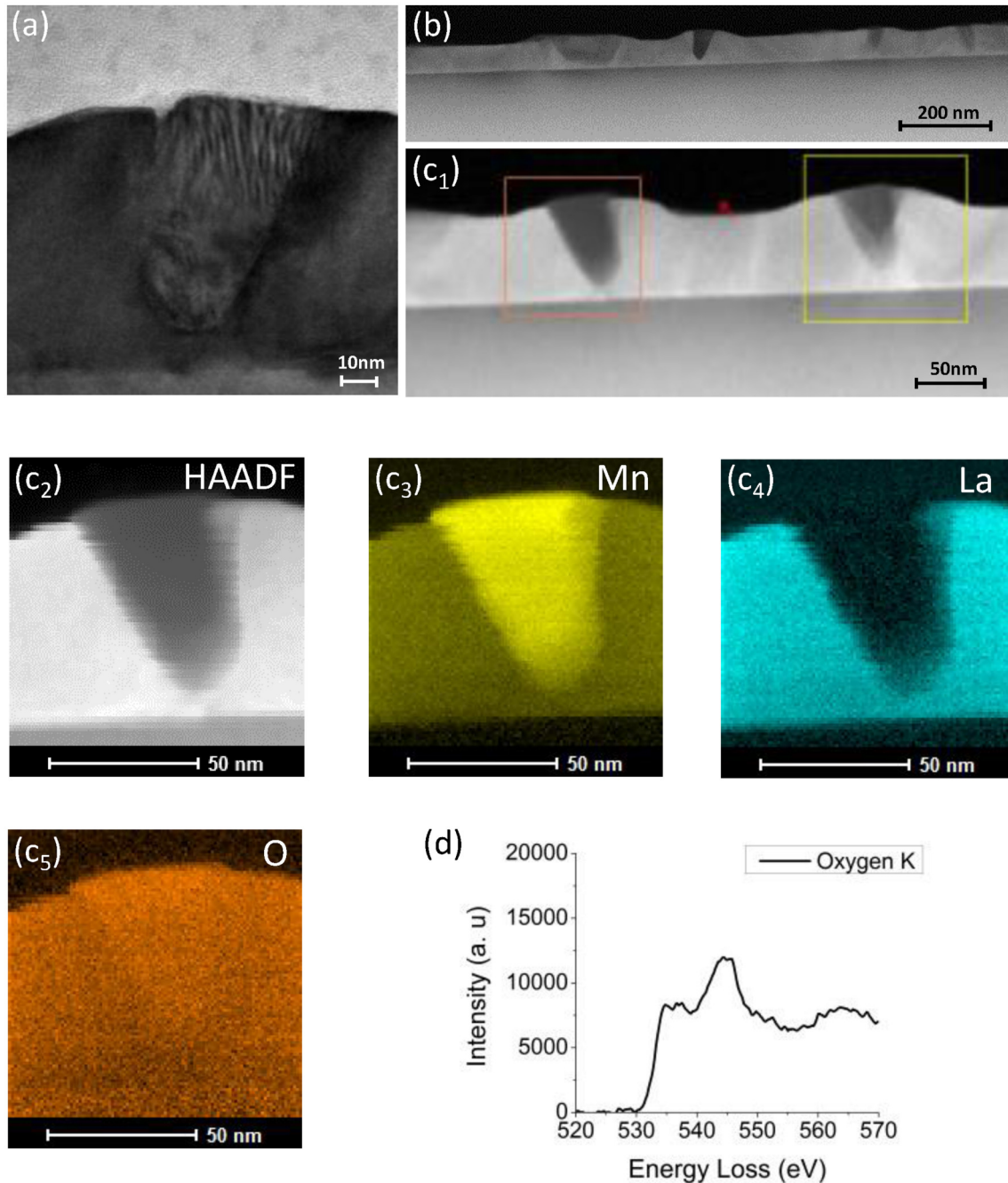
**FIGURE 6 | TEM images of 40 nm LMO thick film grown on STO (A) TEM image around a MnOx inclusion (B) HAADF image of the film (C) EELS mapping: (c1) HAADF image where orange square indicate the zone of the mapping and yellow square is drift correction reference, (c2) Z-contrast image used as a reference for the maps: (c3) manganese energy windows, (c4) lanthanum energy windows, and (c5) oxygen energy window. (D)** Oxygen K edge EELS corresponding to MnO$_x$ nanocolumn obtained from EELS-SI in DualEELS mode.

is a thin LMO matrix layer of around 5 nm (**Figure 6**). Taking into account the huge lattice mismatch between manganese oxide and substrate, it looks energetically unfavorable to nucleate directly on top of the substrate and, instead, a thin LMO layer could act as an efficient buffer layer for drastically decreasing the strain. HAADF images (Z- contrast images) presented in **Figure 6C** show a different contrast between matrix (bright contrast) and nanopillar (dark contrast) indicating different cation composition. Specifically, the chemical analysis, EDS profiles and EELS maps, reveals that the dark zones in HAADF image correspond to a pure manganese oxide whereas the bright zone corresponds to LMO matrix with ratio La/Mn~1. It is noticeable the absence of La inside the inclusions. The analyses of HRTEM images of these nanopillars indicate that manganese oxide has a spinel crystal structure (compatible with Mn$_3$O$_4$) with interplanar distances of 5.2 Å in-plane and of 9.2 Å out-of-plane. Further confirmation that nanoinclusions may be associated to Mn$_3$O$_4$ phase was obtained by studying the oxygen coordination by EELS. **Figure 6D** shows the oxygen K edge EELS spectrum obtained at the nanoinclusions. By comparing this result with the EELS spectrum seies of the manganese oxides reported in literature, the best agreement is found for the Mn$_3$O$_4$ phase [55, 56].
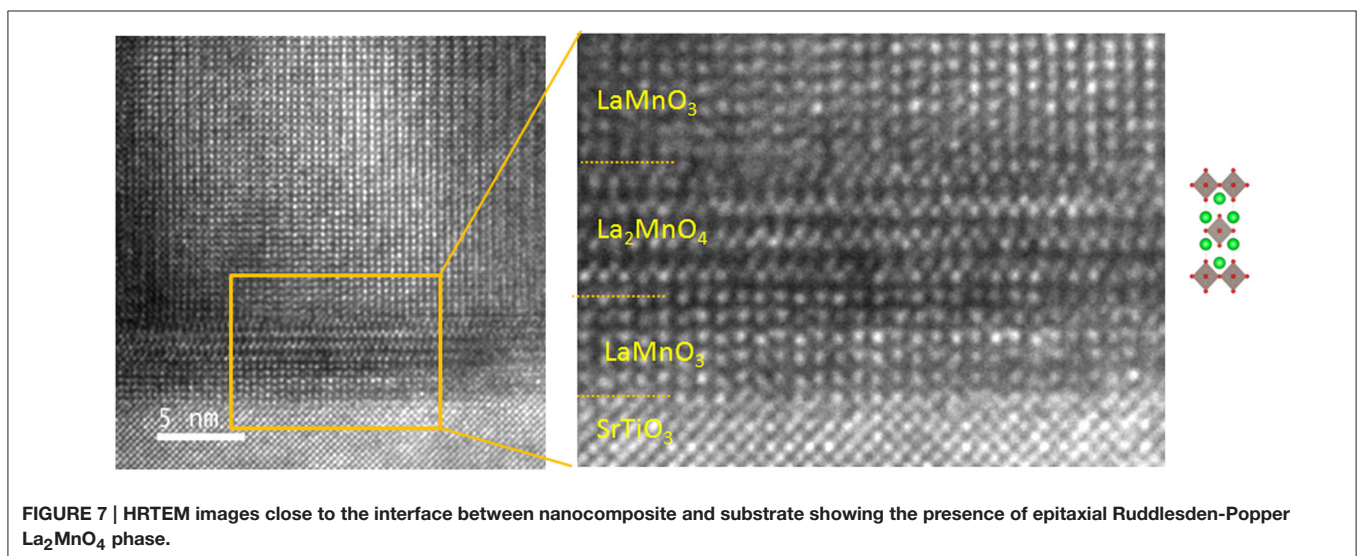
With respect to the perovskite substrate, all precipitates exhibit a similar crystallographic orientation that may be understood in terms of a distorted cubic spinel. Epitaxy may be defined as (001)-oriented cube-on-diagonal (i.e., in-plane rotation of 45°) but with a slight c-axis tilting of 9°, in agreement with the above x-ray diffraction results. HRTEM images (**Figure 6**) also show that interfaces between LMO and Mn$_3$O$_4$ inclusions are not flat, making difficult to define any contact plane. We should note that zig-zag interfaces between Mn$_3$O$_4$ films and manganese perovskite films (in that case La$_{0.7}$Sr$_{0.3}$MnO$_3$) have been previously reported [57], suggesting a tendency in this system to avoid flat interfaces. Nevertheless, statistical analysis shows a tendency to form angles of 35 and 10° with the vertical at both sides of the inclusion. These angles are independent of the surrounding LMO orientation. This suggests

that shape of the inclusions is completely determined during nucleation and growth at the high temperature stage, regardless of their relative orientation with the twinned LMO domains formed during cooling. The other relevant feature identified by HRTEM images and spectroscopy (EDS and EELS) analysis is the presence of an epitaxial (001)-oriented layer of a La-rich secondary phase. This layer is not directly at the interface with the substrate but embedded in the LMO matrix (see **Figure 7**). This secondary phase, of around 2–4 nm thick, has interplanar distances of 3.94 Å in-plane and 13.5 Å out-of-plane and may correspond to the rarely observed Ruddlesden-Popper La$_2$MnO$_4$ phase [14].
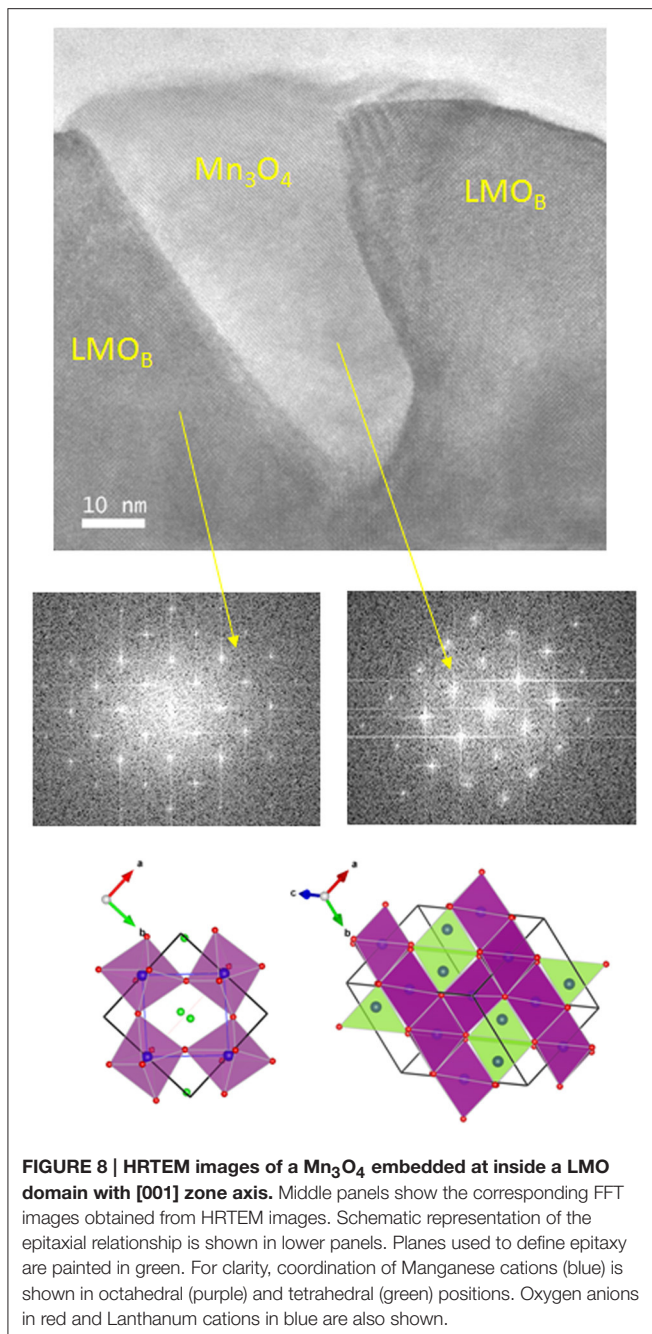
The presence of twin domains in LMO has been also confirmed by cross-section analyses as two different orientations of LMO were identified, i.e., if zone axis is [001]$_{LMO}$ (noted as LMO$_B$) or [110]$_{LMO}$ (noted as LMO$_A$). As the Mn$_3$O$_4$ inclusions are significantly elongated, especially for LMO grown on STO (aspect ratio ~1.7) it is interesting to determine the relative orientation of their long side with respect to the LMO matrix axis. Surprisingly, we have only observed Mn$_3$O$_4$ inclusions with their long side aligned with [001]$_{LMO}$ (see **Figure 8**) or at the interface between [001]$_{LMO}$ or [110]$_{LMO}$ domains (see **Figure 9**). We have not identified inclusions with long axis fully embedded in [110]$_{LMO}$ domains. The epitaxial orientation of the precipitates was determined by analyzing electron diffraction FFT images (middle panels in **Figures 8**, **9**) and by taking hausmannite I4$_1$/amd crystal structure for Mn$_3$O$_4$. Although not strictly parallel (disorientations angle between planes are ~1.5–2°) the most accurate description for the corresponding epitaxial relationships are the following:

$$LMO_A(-11-2)[110]//Mn_3O_4(-202)[010]//LMO_B(100)[001]$$
$$LMO_B(010)[001]//Mn_3O_4(01-1)[111]$$
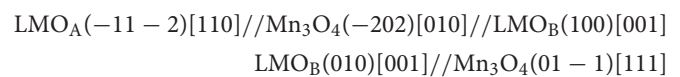
The lower panels in **Figures 8**, **9** are schematized representations of both epitaxial relationships where, for clarity, the defining planes are painted in green.

FIGURE 7 | HRTEM images close to the interface between nanocomposite and substrate showing the presence of epitaxial Ruddlesden-Popper La$_2$MnO$_4$ phase.

FIGURE 8 | HRTEM images of a Mn$_3$O$_4$ embedded at inside a LMO domain with [001] zone axis. Middle panels show the corresponding FFT images obtained from HRTEM images. Schematic representation of the epitaxial relationship is shown in lower panels. Planes used to define epitaxy are painted in green. For clarity, coordination of Manganese cations (blue) is shown in octahedral (purple) and tetrahedral (green) positions. Oxygen anions in red and Lanthanum cations in blue are also shown.

Chemical phase segregation is a complex problem that involves not only thermodynamic stability of the different phases but also kinetic considerations. In general, segregation occurs when the energy cost associated with the creation of new interface and contact area is overcome by the gain in free energy by nucleating a stable secondary phase. Furthermore, in epitaxial thin films, strain associated with the mismatch between lattice parameters of film phases and substrate play an important role and segregates with selected composition may occur to minimize the overall elastic energy of the film. Previous investigations have demonstrated that such mechanism may explain the

occurrence of a three phase oxide manganese nanocomposite similar to our present case [58–60]. In those works, stoichiometry unbalance caused by the spontaneous outcropping of La-Sr-O islands during the growth of $La_{1-x}Sr_xMnO_3$ (LSMO) films is compensated by the appearance of a $Sr_3Mn_2O_7$ Ruddlesden-Popper phase. The main difference in our present study is that LMO films are almost relaxed while formation of La-Sr-O islands helped to maintain LSMO fully strained state. Thus, in LMO films, the energy gain associated with reducing the overall elastic energy of the nanocomposite should be less important than the thermodynamic tendency to form Mn^{2+} ions. It is worth noting that outcropping of secondary phase islands toward the surface of the film is governed by misfit relaxation mechanisms and the resulting topological distribution depends on film thickness and kinetic effects [59]. As a consequence, secondary phases well embedded in the matrix or outcropped toward the surface could just reflect different evolution stages of a similar segregation mechanism.

We have mentioned above that phase diagram of manganese oxides indicates a strong tendency of manganese to adopt an oxidation state of Mn^{2+} in the vacuum conditions (residual oxygen) used to grow the LMO films. The crystal radius of Mn^{2+} in octahedral coordination is 0.97 Å and, attending to the cation radius and the Goldschmidt tolerance factor for perovskites, it could be feasible for Mn to occupy the La site (La^{3+} radius being 1.172 Å) in the LMO perovskite up to the solubility ratio [14]. This mechanism has been reported for La-deficient thin films [61, 62] but, in stoichiometric films should lead to the formation of La-based oxides as La_2O_3 [14] not present in our films. Furthermore, TEM and Raman measurements suggest that LMO matrix preserves [La]/[Mn] ∼ 1. Thus, in the present case, the main mechanism to accommodate Mn^{2+} ions is to form Mn_3O_4 segregates (i.e., $Mn^{2+}[Mn^{3+}]_2O_4$) and the creation of a La-rich phase as the observed La_2MnO_4 phase helps to compensate the stoichiometry unbalance. It is very likely that Mn_3O_4 particles are formed on LMO films during growth process. At that stage, cube-on-cube nucleation of the Mn_3O_4 spinel on the metrically cubic LMO is plausible. The crystallite Mn_3O_4 shape may now be seen as a reminiscence or truncated form of the typical octahedral crystal shape of spinels where {111} surfaces (forming an angle of ∼35° with the vertical) have the lowest surface energy. It is not difficult now to argue that during cooling, when LMO Jahn-Teller transition takes place, Mn_3O_4 accommodates to the surrounding LMO twins by distorting its own structure. The two epitaxial relationships of hausmannite Mn_3O_4 with LMO at room temperature could be just the result of the loss of cubic symmetry, probably linked to distortions originated itself by the Mn^{3+} ion in the octahedral positions of Mn_3O_4. Thus, to fully understand this mechanism, it could be very interesting then to obtain structural information of these nanocomposites at high temperature, namely above T_{JT}.

Temperature dependence at 0.5 T (A) and magnetic field dependence at 10 K

The temperature and the magnetic field dependence of the in-plane magnetization were used to study the effects of the secondary phase on the magnetic properties (**Figure 10**). The temperature dependence of magnetization (in a magnetic field
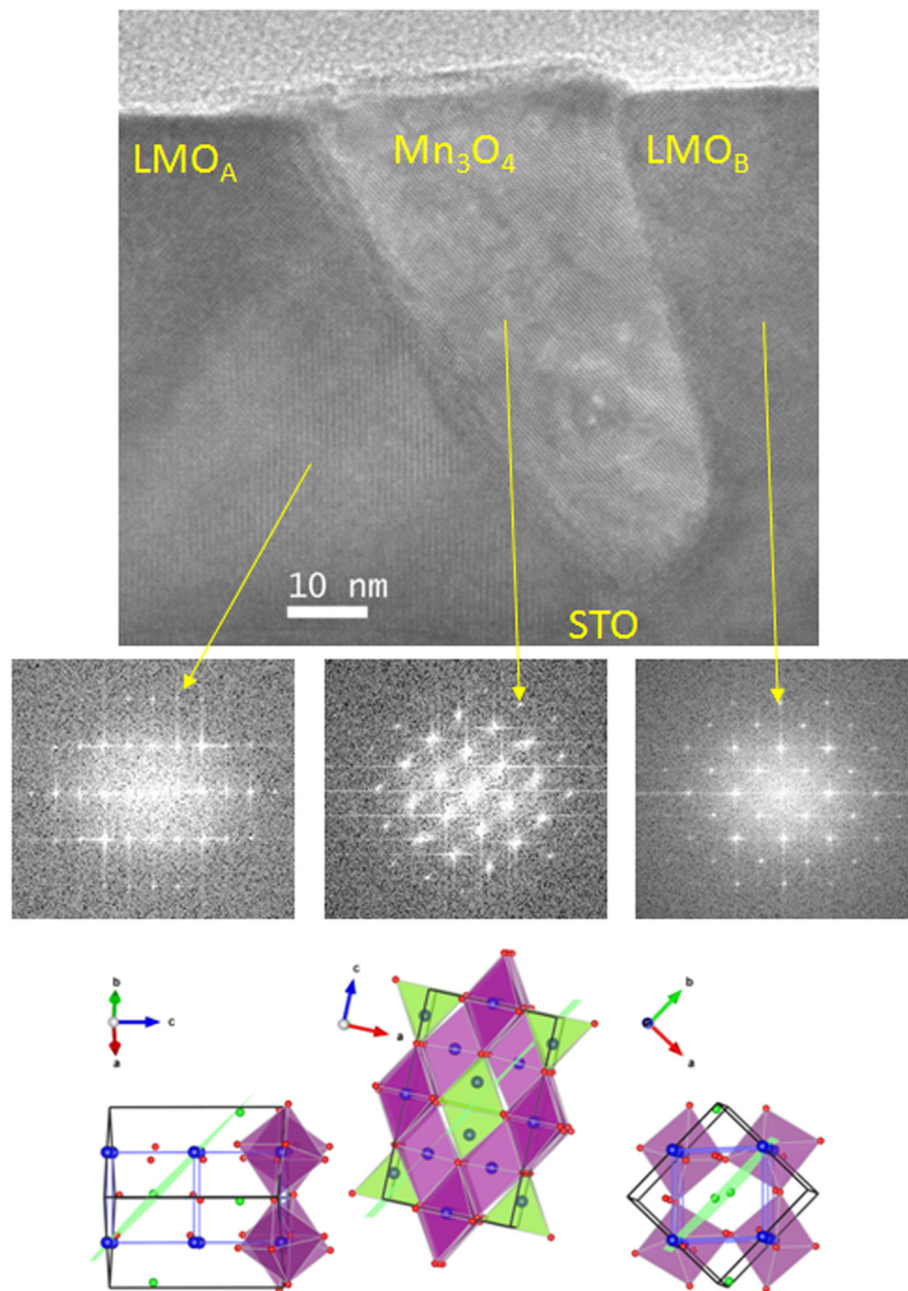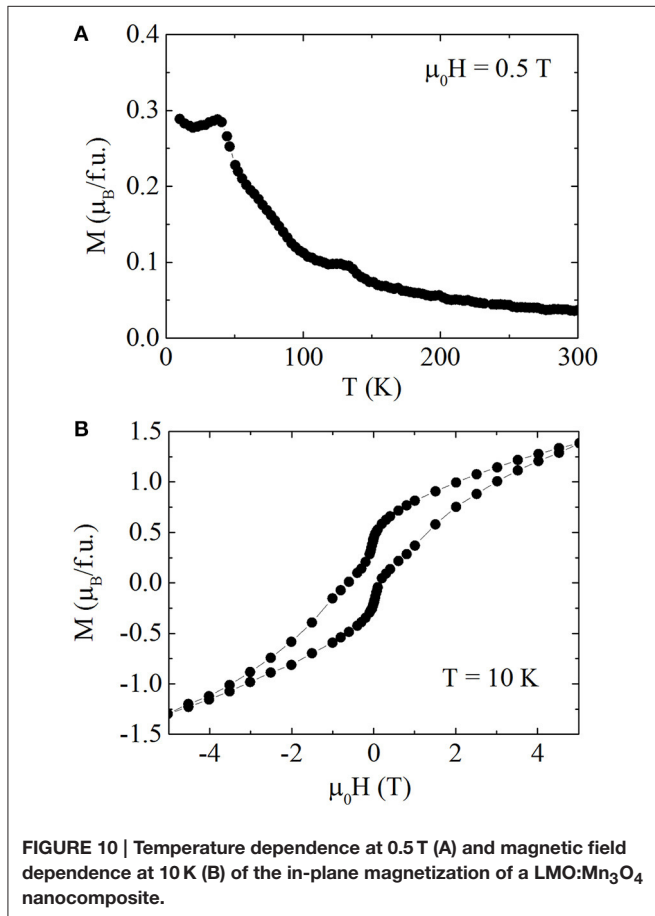
FIGURE 9 | HRTEM images of a Mn₃O₄ embedded at the interface between LMO domains with [001] or [110] zone axis. Middle panels show the corresponding FFT images obtained from HRTEM images. Schematic representation of the epitaxial relationship is shown in lower panels. Planes used to define epitaxy are painted in green. For clarity, coordination of manganese cations (blue) is shown in octahedral (purple) and tetrahedral (green) positions. Oxygen anions in red and Lanthanum cations in blue are also shown.

of 0.1 T) revealed two transitions, the first one is the expected antiferromagnetic transition of LMO at ∼140 K and the second one is the ferrimagnetic transition of manganese oxide secondary phase at around ∼40 K (**Figure 10A**). It is known that LMO thin films may exhibit a broad range of magnetic behaviors, from antiferromagnetic to strongly ferromagnetic, depending on the preparation conditions [27]. In our case, films are prepared

in vacuum conditions leading to a residual moment below 0.3 μ_B/f.u. at 10 K which approaches the bulk value reported in the literature [63]. This residual magnetization is usually associated to a canted antiferromagnetic structure (magnetic moments pointing along b-axis but at a small angle out of ab-plane). The hysteresis loop at 10 K (**Figure 10B**) exhibits typical features observed in loops of thin films composed of soft magnet

with small H$_c$ and hard magnet with larger H$_c$ [12]. However, pure antiferromagnetic LMO thin films shows almost closed hysteresis loop with a very small coercive field H$_c$ that is usually associated to the existence of uncompensated spins at interfaces. On the other hand, manganese oxide with spinel structure is a hard ferrimagnetic with large values of $\mu_0 H_c \sim 0.35$ T [64], whose presence in LMO matrix enlarges loop shape in our system comparing with pure undoped manganite compound.
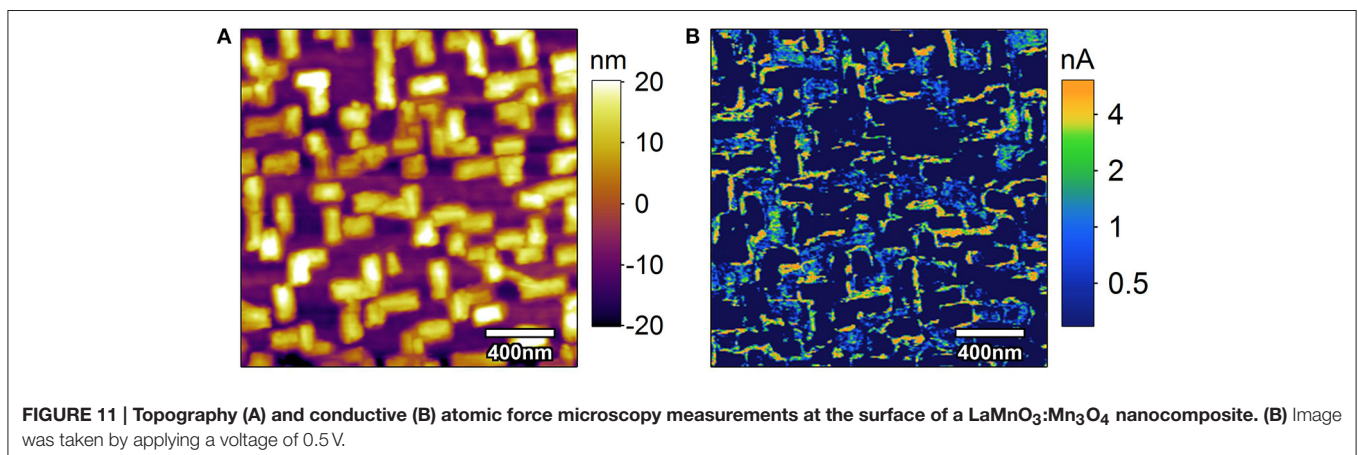

FIGURE 10 | Temperature dependence at 0.5 T (A) and magnetic field dependence at 10 K (B) of the in-plane magnetization of a LMO:Mn$_3$O$_4$ nanocomposite.

The presence of disordered phase boundaries between LMO and Mn$_3$O$_4$ and the larger vertical strain could additionally increase the pinning effects and coercivity in thin films [11].

Effects of secondary phase are revealed also by the local transport measurements shown in **Figure 11**. Characterization is performed by conductive AFM (cAFM) which senses the current flowing from a metallic probe to Pt electrodes deposited on top of the sample. The Mn$_3$O$_4$ secondary phase is highly insulating. However, we observe large spatial differences of the current distribution within the LMO matrix. The overall LMO primary phase in regions between inclusions shows some conduction of the order of few nA for an applied voltage of 0.5 V. Particularly, we observe that conduction is enhanced at the interface region of LMO in close proximity to the inclusions (up to a factor of 10 in these experimental conditions). Moreover, it seems that we observe that not all the four sides of each inclusion are equally conductive. This fact could be supported by TEM cross section images in **Figures 6–9**, showing that nanostructures exhibit a quite asymmetrical shape and thus, conduction could be differently affected at both sides of the inclusion. The driving force for the enhanced conductivity at these interfaces is far from being understood. Several mechanisms are known to increase electrical conductivity of LMO films as, for example, cationic vacancies or oxygen diffusion. Also, the effect on electrical conductivity of local strain fields is quite relevant in oxide thin films and it cannot be disregarded to explain the results in **Figure 11**. However, a deeper study of the transport mechanisms is beyond the scope of this manuscript.

CONCLUSIONS

In conclusion, we report the formation of self-organized Mn$_3$O$_4$ nanocolumns in Pulsed Laser Deposited LaMnO$_3$ films. We show that under vacuum growth conditions there is a strong tendency to form Mn^{2+} cations leading to the segregation of wedge-like Mn$_3$O$_4$ inclusions aligned with the main axis of the substrate. Formation mechanism at high temperatures (850°C) may be understood by considering that Mn$_3$O$_4$ nucleate directly

FIGURE 11 | Topography (A) and conductive (B) atomic force microscopy measurements at the surface of a LaMnO$_3$:Mn$_3$O$_4$ nanocomposite. (B) Image was taken by applying a voltage of 0.5 V.

on the nearly cubic LMO matrix. The final epitaxial relationship is determined by the subsequent Jahn-Teller transition that takes place during cooling creating LMO domains and twins and it may be defined as a distorted cubic spinel with c-axis slightly tilted from the direction perpendicular to the film plane. Partial accommodation of off-stoichiometry and residual strain may be achieved by the creation of an epitaxial La-rich Ruddlesden-Popper La$_2$MnO$_4$ phase close to the interface with the substrate. The magnetic and transport properties of the nanocomposite are strongly modified by the presence of the inclusions. In particular, an enhanced coercivity together with an increase of local conductivity close to the insulating inclusions has been observed. Our results demonstrate an easy single-step route for the preparation of nanocomposite thin films with tuned functional properties consisting of self-assembled ordered nanostructures embedded in a matrix that still preserves its structural characteristics.

AUTHORS CONTRIBUTIONS

AP, ZK, and JS leaded the research, data interpretation and manuscript preparation. NL, MS, and ZP were responsible for Raman results. NB, FS, and JS were responsible for microstructural analysis. LL, LB, AP, ZK, NM, CF, and BM contributed to the initial structural characterization and to the magnetic and c-AFM measurements. JR, AG, AP, and JS were responsible for sample preparation. AP was responsible for preparing the final version of the manuscript that includes the inputs and comments of all the authors.

ACKNOWLEDGMENTS

REFERENCES

1. Choi WS, Kwon JH, Jeen H, Hamann-Borrero JE, Radi A, Macke S, et al. Strain-induced spin states in atomically ordered cobaltites. *Nano Lett.* (2012) **12**:4966–70. doi: 10.1021/nl302562f

2. Vaz CAF. Electric field control of magnetism in multiferroic heterostructures. *J Phys Condens Matter* (2012) **24**:333201. doi: 10.1088/0953-8984/24/33/333201

3. Pomar A, Santiso J, Sandiumenge F, Roqueta J, Bozzo B, Frontera C. et al. Growth kinetics engineered magnetoresistance response in La$_{2/3}$Sr$_{1/3}$MnO$_3$ thin films. *Appl Phys Lett.* (2014) **104**:152406. doi: 10.1063/1.4871984

4. Sandiumenge F, Bagués N, Santiso J, Paradinas M, Pomar A, Konstantinovic Z, et al. Misfit dislocation guided topographic and conduction patterning in complex oxide epitaxial thin films. *Adv Mater Interfaces* (2016) **3**:1600106. doi: 10.1002/admi.201600106

5. Garcia-Barriocanal J, Bruno FY, Rivera-Calzada A, Sefrioui Z, Nemes NM, Garcia-Hernández M, et al. "Charge leakage" at LaMnO$_3$/SrTiO$_3$ interfaces. *Adv Mater.* (2010) **22**:627–32. doi: 10.1002/adma.200902263

6. Bhattacharya A, May SJ, te Velthuis SGE, Warusawithana M, Zhai X, Jiang B, et al. Metal-insulator transition and its relation to magnetic structure in (LaMnO$_3$)$_{2n}$/(SrMnO$_3$)$_n$} superlattices. *Phys Rev Lett.* (2008) **100**:257203. doi: 10.1103/PhysRevLett.100.257203

7. Gibert M, Zubko P, Scherwitzl R, Íñiguez J, Triscone JM. Exchange bias in LaNiO$_3$–LaMnO$_3$ superlattices. *Nat Mater.* (2012) **11**:195–8. doi: 10.1038/nmat3224

8. MacManus-Driscoll JL. Self-assembled heteroepitaxial oxide nanocomposite thin film structures: designing interface-induced functionality in electronic materials. *Adv Funct Mater.* (2010) **20**:2035–45. doi: 10.1002/adfm.201000373

9. Moshnyaga V, Damaschke B, Shapoval O, Belenchuk A, Faupel J, Lebedev OI, et al. Structural phase transition at the percolation threshold in epitaxial (La$_{0.7}$Ca$_{0.3}$MnO$_3$)$_{1-x}$:(MgO)$_x$ nanocomposite films. *Nat Mater.* (2003) **2**:247–52. doi: 10.1038/nmat859

10. Aiping C, Zhenxing B, Harshad H, Xinghang Z, Qing S, Li C, et al. Microstructure, magnetic, and low-field magnetotransport properties of self-assembled (La$_{0.7}$Sr$_{0.3}$MnO$_3$)$_{0.5}$:(CeO$_2$)$_{0.5}$ vertically aligned nanocomposite thin films. *Nanotechnology* (2011) **22**:315712. doi: 10.1088/0957-4484/22/31/315712

11. Chen A, Bi Z, Tsai CF, Lee J, Su Q, Zhang X, et al. Tunable low-field magnetoresistance in (La$_{0.7}$Sr$_{0.3}$MnO$_3$)$_{0.5}$:(ZnO)$_{0.5}$ self-assembled vertically aligned nanocomposite thin films. *Adv Funct Mater.* (2011) **21**:2423–9. doi: 10.1002/adfm.201002746

12. Mukherjee D, Bingham N, Hordagoda M, Phan MH, Srikanth H, Witanachchi S, et al. Influence of microstructure and interfacial strain on the magnetic properties of epitaxial Mn$_3$O$_4$/La$_{0.7}$Sr$_{0.3}$MnO$_3$ layered-composite thin films. *J Appl Phys.* (2012a) **112**:083910. doi: 10.1063/1.4759237

13. Jian H, Zhang Z, Wang Y, Tang X, Yang J, Hu L, et al. Preparation of La$_{0.7}$Sr$_{0.3}$Mn$_{1+x}$O$_y$ (1 < x < 4) thin films by chemical solution deposition: dual epitaxy and possible spinodal growth. *J Alloys Compd.* (2013) **561**:95–100. doi: 10.1016/j.jallcom.2013.02.004

14. Grundy AN, Chen M, Hallstedt B, Gauckler LJ. Assessment of the La-Mn-O system. *J Phase Equilb Diff.* (2005) **26**:131–51. doi: 10.1007/s11669-005-0132-2

15. Joy PA, Sankar CR, Date SK. The limiting value of x in the ferromagnetic compositions La$_{1-x}$MnO$_3$. *J Phys Condens Matter* (2002) **14**:L663. doi: 10.1088/0953-8984/14/39/104

16. Dezanneau G, Audier M, Vincent H, Meneghini C, Djurado E. Structural characterization of La$_{1-x}$MnO$_{3\pm\delta}$ by x-ray diffraction and x-ray absorption spectroscopy. *Phys Rev B* (2004) **69**:11. doi: 10.1103/PhysRevB.69.014412

17. Bosak A, Dubourdieu C, Audier M, Sénateur JP, Pierre J. Compositional effects on the structure and magnetotransport properties of lacunar La$_{1-x}$MnO$_{3-\delta}$ films (x>0) grown by MOCVD. *Appl Phys A* (2004) **79**:1979–84. doi: 10.1007/s00339-003-2179-4

18. Jehanathan N, Lebedev O, Gelard I, Dubourdieu C, Van Tendeloo G. Structure and defect characterization of multiferroic ReMnO$_3$ films and multilayers by TEM. *Nanotechnology* (2010) **21**:075705. doi: 10.1088/0957-4484/21/7/075705

19. Gelard I, Jehanathan N, Roussel H, Gariglio S, Lebedev OI, Van Tendeloo G, et al. Off-stoichiometry effects on the crystalline and defect structure of hexagonal manganite REMnO$_3$ films (RE = V, Er, Dy). *Chem Mater.* (2011) **23**:1232–8. doi: 10.1021/cm1029358

20. Wunderlich R, Chiliotte C, Bridoux G, Maity T, Kocabiyik O, Setzer A, et al. Structural, magnetic and electric properties of HoMnO$_3$ films on SrTiO$_3$(001).

J Magn Magn Mater. (2012) **324**:460–5. doi: 10.1016/j.jmmm.2011.08.021

21. Tian ZR, Tong W, Wang JY, Duan NG, Krishnan VV, Suib SL. Manganese oxide mesoporous structures: mixed-valent semiconducting catalysts. *Science* (1997) **276**:926–30. doi: 10.1126/science.276.5314.926

22. Zhang L, Zhou Q, Liu Z, Hou X, Li Y, Lv Y. Novel Mn$_3$O$_4$ micro-octahedra: promising cataluminescence sensing material for acetone. *Chem Mater.* (2009) **21**:5066–71. doi: 10.1021/cm901369u

23. Najafpour MM, Holynska M, Salimi S. Applications of the "nano to bulk" Mn oxides: Mn oxide as a Swiss army knife. *Coord Chem Rev.* (2015) **285**:65–75. doi: 10.1016/j.ccr.2014.11.001

24. Najafpour MM, Renger G, Holynska M, Moghaddam AN, Aro EM, Carpentier R, et al. Manganese compounds as water-oxidizing catalysts: from the natural water-oxidizing complex to nanosized manganese oxide structures. *Chem Rev.* (2016) **116**:2886–936. doi: 10.1021/acs.chemrev.5b00340

25. Huang Q, Santoro, A, Lynn JW, Erwin RW, Borchers JA, Peng JL, et al. Structure and magnetic order in undoped lanthanum manganite. *Phys Rev B* (1997) **55**:14987–99. doi: 10.1103/PhysRevB.55.14987

26. Ritter C, Ibarra MR, De Teresa JM, Algarabel PA, Marquina C, Blasco J, et al. Influence of oxygen content on the structural, magnetotransport, and magnetic properties of LaMnO$_{3+\delta}$. *Phys Rev B* (1997) **56**:8902–11. doi: 10.1103/PhysRevB.56.8902

27. Roqueta J, Pomar A, Balcells L, Frontera C, Valencia S, Abrudan R, et al. Strain-engineered ferromagnetism in LaMnO$_3$ thin films. *Cryst Growth Des.* (2015) **15**:5332–7. doi: 10.1021/acs.cgd.5b00884

28. Marton Z, Seo SSA, Egami T, Lee HN. Growth control of stoichiometry in LaMnO$_3$ epitaxial thin films by pulsed laser deposition. *J Cryst Growth* (2010) **312**:2923–7. doi: 10.1016/j.jcrysgro.2010.07.013

29. Marozau I, Das PT, Dobeli M, Storey JG, Uribe-Laverde MA, Das S, et al. Influence of La and Mn vacancies on the electronic and magnetic properties of LaMnO$_3$ thin films grown by pulsed laser deposition. *Phys Rev B* (2014) **89**:174422. doi: 10.1103/PhysRevB.89.174422

30. Kim SH, Choi BJ, Lee GH, Oh SJ, Kim B, Choi HC, et al. Ferrimagnetism in γ-manganese sesquioxide (γ-Mn$_2$O$_3$) nanoparticles. *J Korean Phys Soc.* (2005) **46**:941. doi: 10.3938/jkps.46.491

31. Fritsch S, Navrotsky A. Thermodynamic properties of manganese oxides. *J Am Ceram Soc.* (1996) **79**:1761–8. doi: 10.1111/j.1151-2916.1996.tb07993.x

32. Grant RW, Geller S, Cape JA, Espinosa GP. Magnetic and crystallographic transitions in α-Mn$_2$O$_3$-Fe$_2$O$_3$ system. *Phys Rev.* (1968) **175**:686. doi: 10.1103/PhysRev.175.686

33. Boucher B, Buhl R, Perrin M. Magnetic structure of Mn$_3$O$_4$ by neutron diffraction. *J Appl Phys.* (1971) **42**:1615–7. doi: 10.1063/1.1660364

34. Radler MJ, Cohen JB, Sykora GP, Mason T, Ellis DE, Faber J. The defect structures of Mn$_{1-x}$O. *J Phys Chem Solids* (1992) **53**:141–54. doi: 10.1016/0022-3697(92)90022-6

35. Aminoff G. On the crystal structure of hausmannite (MnMn$_2$O$_4$). *Z Kristallogr.* (1926) **64**:475–90.

36. Baron V, Gutzmer J, Rundlof H, Tellgren R. The influence of iron substitution on the magnetic properties of hausmannite, Mn^{2+}(Fe,Mn)$_2^{3+}$O$_4$. *Am Mineral.* (1998) **83**:786–93. doi: 10.2138/am-1998-7-810

37. Ross CR, Rubie DC., Paris E. Rietveld refinement of the high-pressure polymorph of Mn$_3$O$_4$. *Am Mineral.* (1990) **75**:1249–52.

38. Gorbenko OY, Samoilenkov SV, Graboy IE, Kaul AR. Epitaxial stabilization of oxides in thin films. *Chem Mater.* (2002b) **14**:4026–43. doi: 10.1021/cm021111v

39. Kaul AR, Gorbenko OY, Graboy IE, Samoilenkov SV. Epitaxial stabilization of oxide phases in thin film growth. In: Guilloux-Viry M, Perrin A, editors. *Cryst Growth Thin Solid Films*. Trivandrum: Research SignPost (2002), 265–94.

40. Gorbenko OY, Graboy IE, Amelichev VA, Bosak AA, Kaul AR, Guttler B, et al. The structure and properties of Mn$_3$O$_4$ thin films grown by MOCVD. *Solid State Commun.* (2002a) **124**:15–20. doi: 10.1016/S0038-1098(02)00470-2

41. Bi Z, Weal E, Luo H, Chen A, MacManus-Driscoll JL, Jia Q, et al. Microstructural and magnetic properties of (La$_{0.7}$Sr$_{0.3}$MnO$_3$)$_{0.7}$:(Mn$_3$O$_4$)$_{0.3}$ nanocomposite thin films. *J Appl Phys.* (2011) **109**:054302. doi: 10.1063/1.3552594

42. Momma K, Izumi F. VESTA 3 for three-dimensional visualization of crystal, volumetric and morphology data. *J Appl Crystallogr.* (2011) **44**:1272–6. doi: 10.1107/S0021889811038970

43. Lucas G, Burdet P, Cantoni M, Hebert C. Multivariate statistical analysis as a tool for the segmentation of 3D spectral data. *Micron* (2013) **52–53**:49–56. doi: 10.1016/j.micron.2013.08.005

44. Bernal S, Botana FJ, Calvino JJ, Lopez-Cartes C, Perez-Omil JA, Rodriguez-Izquierdo JM. The interpretation of HREM images of supported metal catalysts using image simulation: profile view images. *Ultramicroscopy* (1998) **72**:135–64. doi: 10.1016/S0304-3991(98)00009-6

45. Aruta C, Angeloni M, Balestrino G, Boggio NG, Medaglia PG, Tebano A, et al. Preparation and characterization of LaMnO$_3$ thin films grown by pulsed laser deposition. *J Appl Phys.* (2006) **100**:023910. doi: 10.1063/1.2217983

46. Choi WS, Marton Z, Jang SY, Moon SJ, Jeon BC, Shin JH, et al. Effects of oxygen-reducing atmosphere annealing on LaMnO$_3$ epitaxial thin films. *J Phys D Appl Phys.* (2009) **42**:165401. doi: 10.1088/0022-3727/42/16/165401

47. Orgiani P, Aruta C, Ciancio R, Galdi A, Maritato L. Enhanced transport properties in La$_x$MnO$_{3-\delta}$ thin films epitaxially grown on SrTiO$_3$ substrates: the profound impact of the oxygen content. *Appl Phys Lett.* (2009) **95**:013510. doi: 10.1063/1.3168649

48. Kim HS, Christen HM. Controlling the magnetic properties of LaMnO$_3$ thin films on SrTiO$_3$(100) by deposition in a O$_2$/Ar gas mixture. *J Phys Condens Matter* (2010) **22**:146007. doi: 10.1088/0953-8984/22/14/146007

49. Choi WS, Jeong DW, Jang SY, Marton Z, Seo SSA, Lee HN, et al. LaMnO$_3$ thin films grown by using pulsed laser deposition and their simple recovery to a stoichiometric phase by annealing. *J Korean Phys Soc.* (2011) **58**:569–74. doi: 10.3938/jkps.58.569

50. Rodriguez-Carvajal J, Hennion M, Moussa F, Moudden AH, Pinsard L, Revcolevschi A. Neutron-diffraction study of the Jahn-Teller transition in stoichiometric LaMnO$_3$. *Phys Rev B* (1998) **57**:R3189–92. doi: 10.1103/PhysRevB.57.R3189

51. Iliev MN, Abrashev MV, Lee HG, Popov VN, Sun YY, Thomsen C, et al. Raman spectroscopy of orthorhombic perovskitelike YMnO$_3$ and LaMnO$_3$. *Phys Rev B* (1998) **57**:2872–7. doi: 10.1103/PhysRevB.57.2872

52. Iliev MN, Abrashev MV. Raman phonons and Raman Jahn-Teller bands in perovskite-like manganites. *J Raman Spectrosc.* (2001) **32**:805–11. doi: 10.1002/jrs.770

53. Zuo J, Xu CY, Liu YP, Qian YT. Crystallite size effects on the Raman spectra of Mn$_3$O$_4$. *Nanostruct Mater.* (1998) **10**:1331–5. doi: 10.1016/S0965-9773(99)00002-1

54. Julien CM, Massot M, Poinsignon C. Lattice vibrations of manganese oxides. Part I. *Periodic structures. Spectrochim Acta Part A Mol Biomol Spectrosc.* (2004) **60**:689–700. doi: 10.1016/S1386-1425(03)00279-8

55. Kurata H, Colliex C. Electron-energy-loss core-edge structures in manganese oxides. *Phys Rev B* (1993) **48**:2102–8. doi: 10.1103/PhysRevB.48.2102

56. Tan HY, Verbeeck J, Abakumov A, Van Tendeloo G. Oxidation state and chemical shift investigation in transition metal oxides by EELS. *Ultramicroscopy* (2012) **116**:24–33. doi: 10.1016/j.ultramic.2012.03.002

57. Mukherjee D, Bingham N, Phan MH, Srikanth H, Mukherjee P, Witanachchi S. Ziz-zag interface and strain-influenced ferromagnetism in epitaxial Mn$_3$O$_4$/La$_{0.7}$Sr$_{0.3}$MnO$_3$ thin films grown on SrTiO$_3$ (100) substrates. *J Appl Phys.* (2012b) **111**:3. doi: 10.1063/1.3680531

58. Moreno C, Abellan P, Hassini A, Ruyter A, Perez del Pino A, Sandiumenge F, et al. Spontaneous outcropping of self-assembled insulating nanodots in solution-derived metallic ferromagnetic La$_{0.7}$Sr$_{0.3}$MnO$_3$ films. *Adv Funct Mater.* (2009) **19**:2139–46. doi: 10.1002/adfm.200900095

59. Abellan P, Moreno C, Sandiumenge F, Obradors X, Casanove MJ. Misfit relaxation of La$_{0.7}$Sr$_{0.3}$MnO$_3$ thin films by a nanodot segregation mechanism. *Appl Phys Lett.* (2011) **98**:041903. doi: 10.1063/1.3549182

60. Moreno C, Abellan P, Sandiumenge F, Casanove MJ, Obradors X. Nanocomposite lanthanum strontium manganite thin films formed by using a chemical solution deposition. *Appl Phys Lett.* (2012) **100**:023103. doi: 10.1063/1.3675461

61. Orgiani P, Galdi A, Aruta C, Cataudella V, De Filippis G, Perroni CA, et al. Multiple double-exchange mechanism by Mn^{2+} doping in manganite compounds. *Phys Rev B* (2010) **82**:205122. doi: 10.1103/PhysRevB.82.205122

62. Orgiani P, Aruta C, Ciancio R, Galdi A, Maritato L. Synthesis and properties of highly metallic orbital-ordered A-site manganites. *J Nanopart Res.* (2013) **15**:1655. doi: 10.1007/s11051-013-1655-9

63. Topfer J, Goodenough JB. $LaMnO_{3+\delta}$ revisited. *J Solid State Chem.* (1997) **130**:117–28.

64. Guo LW, Peng DL, Makino H, Inaba K, Ko HJ, Sumiyama K, et al. Structural and magnetic properties of Mn_3O_4 films grown on MgO(0 0 1) substrates by plasma-assisted MBE. *J Magn Magn Mater.* (2000) **213**:321–5. doi: 10.1016/S0304-8853(00)00008-1